**Made available by Hasselt University Library in https://documentserver.uhasselt.be**

# Graphene Encapsulated Diamond Nanoneedles as Sensitive Electrochemical Paraquat Sensor for Amaranthus Leaves

Peer-reviewed author version

Chaudhary, Yogesh; POBEDINSKAS, Paulius; ROUZBAHANI BAYATANI, Rozita; Korneychuk, Svetlana; VERBEECK, Johan; Sankaran, Kamatchi Jothiramalingam & HAENEN, Ken (2025) Graphene Encapsulated Diamond Nanoneedles as Sensitive Electrochemical Paraquat Sensor for Amaranthus Leaves. In: Langmuir, 41 (24) , p. 15283 -15291.

DOI: 10.1021/acs.langmuir.5c00686
Handle: http://hdl.handle.net/1942/46366

# Graphene Encapsulated Diamond Nanoneedles as Sensitive Electrochemical Paraquat Sensor for *Amaranthus* Leaves

Yogesh Chaudhary[1,2], Paulius Pobedinskas[3], Rozita Rouzbahani[3], Svetlana Korneychuk[4], Johan Verbeeck[4], Kamatchi Jothiramalingam Sankaran[1,2,*], Ken Haenen[3,*]

[1]CSIR-Institute of Minerals and Materials Technology, Bhubaneswar-751013, India;

[2]Academy of Scientific and Innovative Research (AcSIR), Ghaziabad 201002, India;

[3]Institute for Materials Research (IMO), Hasselt University, and IMOMEC, IMEC vzw, 3590 Diepenbeek, Belgium;

[4]Electron Microscopy for Materials Science (EMAT), University of Antwerp, 2020 Antwerp, Belgium.

*Correspondence:* *Kamatchi Jothiramalingam Sankaran; (*kjsankaran@immt.res.in*) and *Ken Haenen (*ken.haenen@uhasselt.be*)

**ABSTRACT:** Ensuring food security often requires the use of pesticides, which can lead to significant ecological and human health risks due to toxicity. Paraquat (PQ), one of the most dangerous herbicides, poses severe threats to human health, including organ failure and neurological damage. Electrochemical detection methods have demonstrated significant promise for accurate and sensitive detection of PQ. Nonetheless, conventional methods for fabricating electrodes are typically complex and time-consuming, which hinders their applicability in fast and efficient sensing systems. In this study, graphene-encapsulated diamond nanoneedles (GDNs) were synthesized as robust electrodes using microwave plasma-enhanced chemical vapor deposition system. The microstructural analysis reveals that the diamond nanoneedles

were encapsulated by graphene sheaths. The GDNs demonstrated desirable conductivity and electrochemical activity, attributed to the coexistence of diamond and graphite phases.

Using these GDN electrodes, differential pulsed anodic stripping voltammetry in a 0.1M phosphate buffer solution enabled impressive detection of PQ, achieving the limit of detection as 0.002 μM and 2.97 μA/μM sensitivity at an optimal condition in the linearity range of 0.1 to 0.8 μM. The electrodes demonstrated high repeatability, selectivity, and remarkable recovery in real samples, including seawater and washed water from Amaranthus leaves, highlighting as a potential sensing material for the real time monitoring of PQ.

## INTRODUCTION

Recent agricultural practices have demonstrated the widespread use of pesticides to maximize crop yields by controlling pests, thus ensuring food security.[1] However, pesticides not only kill pests but also harm the environment and living beings with prolonged exposure. One of the most frequently used pesticides is Paraquat (PQ), (1,1'-dimethyl-4,4'-dipyridinium chloride) also called methyl viologen, a herbicide to control weeds in plantation crops and acts as a desiccant in pre-harvest treatments for horticultural purposes.[2,3] PQ is extremely toxic and persists for a long period in the surroundings.[4] Chronic exposure to PQ severely impacts major human organs, including the heart, kidneys, liver, brain, respiratory system and even causes nervous disorders for instance alzheimer, parkinson and dementia.[5–8] Currently, there is no effective antidote for PQ toxicity when ingested in large quantities.[9] Given the fatal risks and dangers of pesticide poisoning, it is essential to monitor and control PQ residues in water, soil, and food using precise, robust and cost-effective techniques. Various conventional analytical methods [10–14] have been developed for PQ detection. However, these methods typically require sophisticated voluminous instrumentation, trained expertise for sample preparation and analysis,

and are often time-consuming, expensive and thus, making them less suitable for point-of-care applications. In contrast, modern electrochemical detection methods are highly favoured for PQ monitoring due to their rapid response, affordability, high sensitivity and minimal chemical consumption.[1,5,15] This technique offers the advantage of miniaturization, enabling portability, which is rarely possible for such precise on-site monitoring for real samples.[1] The electroanalytical approach uses differential pulsed anodic stripping voltammetry (DPASV), which enhances detection sensitivity by measuring faradic current when capacitive current is minimal, making it appropriate for rapid analysis of environmental contaminants.[16–18] The electrochemical sensing platform utilizes three electrodes set up, among which the working electrode provides the interactive surface for analytes to be detected.

In the search of an efficient electrode for pesticides detection, several electrode fabrication procedures have been adopted by scientists. The majority of studies have concentrated on carbon-based hybrid electrode materials.[19] For example, an electrode (AChE/CNTs–$NH_2$/AgNPs-N-F-$MoS_2$/GCE) was developed to detect chlorpyrifos and monocrotophos with limit of detection of 3 pM, 0.2 pM respectively. Nevertheless, the fabrication process is time-consuming and requires elevated temperatures.[20] In addition to this, a MXene/ERGO/GCE electrochemical sensor, fabricated by HF etching method was used to detect 0.67 nM carbendazim in orange and cucumber samples.[21] With the application in real samples of potatoes and river water, the pesticide carbofuran was electrochemically detected by using a $Gd_2S_3$/RGO/GCE sensor, reaching the detection limit 0.012 μM, with stability 96.28%.[22] Similarly, a g–$C_3N_4$/GO/Fc–TED/GCE sensor through thermal polymerization was developed for detecting 8.3 nM metolcarb in spinach samples with 94.75% stability after 30 days.[23] In addition, a Cu–MOF-based electrode material, N/Cu–MOF/HPC/GCE, has been recently reported by

using a modified thermal processing method for the quantitative detection of 0.026 μM, 0.01μM and 0.062 μM, imidacloprid, dinotefuran and thiamethoxam, respectively in oat and corn samples.[24] MOFs tend to be unstable in aqueous environments, posing challenges for real-time analysis applications. To overcome this, intricate sample pre-treatment steps are typically required. Moreover, a GCE electrode functionalized with pillar arene, graphene oxide and silver nanoparticles detects $10^{-8}$ M PQ detection.[25] However, unmodified GCE and graphene lack sufficient sensitivity detection for effective electrochemical sensing of PQ. Additionally, a GCE was functionalized by polymerizing β-cyclodextrin with citric acid as a crosslinker on the smectite surface, allowing it to detect PQ up to 0.74 μg/L.[26]

Despite of the LODs obtained, they still are below the residual limit of PQ as prescribed by the WHO in food samples. However, fabricating these electrodes involves lengthy modification steps and the use of chemicals, making them less practical and affordable for real-time monitoring. Moreover, the fabrication procedure of these modified electrodes is not reliable to be reproduced to maintain the acceptable value of sensitivity and limit of detection over a long-time usage. Thus, a single-step electrode preparation process would be advantageous in saving time and reducing costs.

In this work, keeping in mind the complexities involved in the above-mentioned fabrication techniques, herein we have fabricated simple and feasible single step graphene encapsulated diamond nanoneedles (GDNs), employing microwave plasma enhanced chemical vapor deposition (MPECVD) system. Since, lab grown diamond-based electrodes are good alternatives for the electrochemical sensing applications because of the lower background current response, large potential window, stability in harsh environments, electrochemical stability, anti-

fouling properties and their robustness.[27] However, the wide band gap, low active surface area, challenges for surface functionalization and slow electron transfer kinetics necessitates to be assisted by electrically conducting materials for electrochemical applications.[28] In contrast, the remarkable electrical conductivity, ease of functionalization and fast electron kinetics characteristics of graphene makes it suitable for electrochemical applications.[29,30] But, the electrode fouling, aggregation of graphene, instability towards environmental factors makes it tricky to be used alone as electrode material.[31] Thus, the combination of both diamond and graphene as a hybrid electrode may provide synergistic effects, which can make them a reliable electrochemical sensor for particularly PQ detection. The applicability of GDN electrodes has been successfully utilized for the electrochemical detection of PQ suppressing the individual materials' weaknesses and enhancing the mutual effects together. Using the DPASV method, the GDNs act as an efficient electrode material with high sensitivity, specificity, repeatability, stability and reproducibility for electroanalytical detection of PQ in real environments. The PQ redox mechanism at the GDNs the is well-elaborated in this study.

## EXPERIMENTAL SECTION

### Synthesis of GDNs

The GDNs were synthesized on (100) silicon substrates using an MWPECVD (ASTeX 6500 series) reactor. The substrates were seeded using a colloidal suspension containing detonation nanodiamonds with sizes ranging from 5 to 7 nm[32]. The followed growth conditions of the GDNs are: a gaseous mixture of $CH_4$ (15%)/$H_2$ (81%)/$N_2$ (4%) =45 sccm/243 sccm/12 sccm of total flow rate 300 sccm, microwave power of 3000 W, pressure of 65 Torr, substrate temperature of 750°C and a growth time of 60 min.

### Reagents

All chemical reagents utilized were of analytical grade and were applied as received. For the electrochemical characterization of GDNs, 5 mM solutions of Potassium ferricyanide ($K_3[Fe(CN)_6]$, 99.0% purity), and potassium ferrocyanide ($K_4Fe(CN)_6 \cdot 3H_2O$, 99.0% purity), procured from Thermo Fisher Scientific Pvt. Ltd., Hyderabad, India, were utilized as redox probes, containing 0.1 M potassium chloride (KCl, 99.5% purity) as the supporting electrolyte. Additional chemicals are sodium phosphate dibasic heptahydrate ($Na_2HPO_4 \cdot 7H_2O$, 98.0 % purity) and sodium phosphate monobasic monohydrate ($NaH_2PO_4 \cdot H_2O$, 98.0 % purity), both sourced from Merck Life Science Pvt. Ltd., Mumbai, India. Paraquat dichloride hydrate (PESTANAL®, ≥98.9% purity) was purchased from Merck Life Science Pvt. Ltd., Darmstadt, Germany.

**Characterization**

The topography and microstructure of the GDNs was analyzed by a FEI Quanta 200 FEG scanning electron microscope performed at an accelerating voltage of 15 kV. The crystalline quality was assessed through Raman spectroscopy, employing a Horiba Jobin Yvon T64000 spectrometer paired with a Horiba JY Symphony CCD detector and a BXFM Olympus 9/128 microscope utilizing a 488 nm Lexell SHG laser. The microstructural features of the GDNs were investigated using a FEI-Titan “cubed” microscope operating at 300 kV for high-angle annular dark-field scanning transmission electron microscopy (HAADF-STEM). The convergence semi-angle (α) used was 22 mrad, and the inner acceptance semi-angle (β) for HAADF-STEM imaging was also 22 mrad. The focused ion beam (FIB) technique was used for the preparation of STEM samples. Additionally, the crystallinity of the GDNs was further examined using X-ray diffraction (XRD) analysis, accomplished on a Malvern Panalytical Aeris diffractometer

(Netherlands) equipped with Cu Kα radiation (λ = 1.5406 Å) conducted over a 2θ range of 10° to 60°.

**Electrochemical Studies**

The portable electrochemical workstation (Palmsens; EmStat-4LR, Netherlands) configured with a three-electrode system was used for carrying out the electrochemical studies. The three-electrode system comprised of Ag/AgCl (3 M KCl) as reference electrode, GDNs as working electrode, and platinum wire as counter electrode. The electrochemical characterizations were performed by cyclic voltammetry (CV) and Electrochemical impedance spectroscopy (EIS). CVs were executed over a potential range of -0.6 V to 1.0 V, with scan rates ranging from 10 to 100 $mV \cdot s^{-1}$. For EIS measurement, the frequency was ranged from 0.01 Hz to 100 kHz, and the EIS data were analyzed by a Randles equivalent circuit through PS Trace software version 5.9. In order to detect PQ in 0.1 M phosphate buffer solution (PBS), DPASV was applied, varying the potential range from -1.0 V to 0.0 V with a potential step at 0.1V, pulse potential at 0.1V, scan rate at 50 $mVs^{-1}$ and pulse duration of 0.02 s. A 0.1M PBS was prepared by dissolving appropriate amounts of $Na_2HPO_4 \cdot 7H_2O$ and $NaH_2PO_4 \cdot H_2O$, with the pH adjusted from 4 to 9 using KOH or HCl as needed. A 1 mM aqueous PQ solution was used as stock solution, stored at 8°C in a refrigerator. The exposed active area of the working electrode (GDNs) is 0.125 $cm^2$.

**RESULTS AND DISCUSSION**

The morphological features of GDNs as displayed in FESEM micrograph of Figure 1a, clearly reveals the formation of 1D nanoneedles. Most of the nanoneedle-like structures oriented randomly with lengths ranging from 200 to 480 nm and diameters measuring only a few nanometres. Moreover, the thickness of the layered GDNs is estimated as an average of 216 nm (inset of Figure 1aI).

Furthermore, Raman measurements were conducted to differentiate various carbonaceous phases (such as diamond, graphite, and amorphous carbon) in the GDNs (Figure 1b). The Raman spectrum ($\lambda$ = 488 nm) of GDNs exhibits the key peaks: D band near 1356 $cm^{-1}$, associated with disordered $sp^3$- carbon that indicates defects present in the carbon structure, G band around 1585 $cm^{-1}$, attributed to the $sp^2$- carbon of $E_{2g}$ phonon modes, and prominent 2D peak near 2713 $cm^{-1}$, arising from a $2^{nd}$-order scattering phenomenon.[33] The $I_{2D}/I_G$ ratio (intensity ratio of 2D band to the G band) is 0.34, suggesting the presence of graphene phases within the GDNs. Furthermore, the D + G band nearly at 2937 $cm^{-1}$ corresponds to the disordered in $sp^2$ domains and along the edges of the graphene in the GDNs. It is reported that the formation of aromatic hydrocarbons that condense on the growing diamond surface, facilitates the creation of $sp^2$ hybridized carbon phases.[34]

The chemical bonding characteristics of GDNs was characterized by XPS. The inset of Figure 1b displays the C1s spectrum of GDNs, deconvoluted into four components comprise: $sp^2$ bonded carbon atoms around ~284.4 eV, (peak intensity of 66.37%), $sp^3$ hybridized carbon atoms peaking at ~284.8 eV (peak intensity of 21.6%), C=N/C-O component at ~286.2 eV (peak intensity of 9.13%) and a weak C=O component at 288.8 eV (peak intensity of 2.9%).[33] The greater intensity of $sp^2$-carbon (C=C) than that of $sp^3$-carbon (C-C) clearly confirms the presence of graphene phases in the GDNs.

The microstructure of the GDNs was examined by the STEM. The cross-sectional bright-field STEM image, presented as an inset of Figure 1c confirms the origin of needle-like diamond grains on the Si substrates. The typical HAADF-STEM displayed in Figure 1d reveals that the needle entails of the diamond grains encapsulated with graphene phases with a thickness ranging

from few layers up to 15 atomic layers. The interface between the diamond grains also contains the graphene phases, denoted by arrows. Moreover, the inset HAADF-STEM from Figure 1d shows the graphene layers mostly grow parallel to the diamond grain's surface. The presence of graphene phases encapsulating diamond needles as observed through STEM analysis is also supported by the Raman and XPS analyses. Figure S1 (supporting information) presents the XRD pattern of GDNs, which clearly shows the characteristic diffraction planes of graphene (002) and diamond (111) phases at 2θ, 26.9° and 43.7° respectively, indicating diamond-graphene mixed phase.[34]

The growth mechanism of GDNs involves the participation of $C_2$ and CN radicals already exist in the plasma, which play crucial role in forming the hybrid nanoneedle structures.[35,36] At high substrate temperature (750°C), the CN species are highly energetic and hence promoting the attachment of $C_2$ species onto surfaces where CN has already adhered. This concurrent incorporation of $C_2$ species, along with the growth of diamond grains anisotropically, leads to the growth of diamond nanoneedles with large aspect ratios. Additionally, in the anisotropic diamond growth, the carbon atoms present on the surface around the $sp^3$-bonded diamond core preferentially transform into $sp^2$-bonded carbon due to energetic favourability, prominent to the evolution of graphene layers that are covalently bonded with diamond.[37,38] These diamond needles encapsulated with graphene exhibit excellent electrical conductivity,[36] making them particularly effective for electrochemical applications. This is largely attributed to their heterogeneous surface, which is enriched with $sp^2$ carbon predominantly located at grain boundaries and defects.[34] Since, $sp^2$ carbon serves as a crucial pathway for charge transfer processes, it can significantly influence the performance of the electrode. The graphene nanostructures and enhanced grain boundaries are expected for the increased surface area of

GDNs, which thereby increases the electrical conductivity. Furthermore, one-dimensional diamond nanoneedles have shown greater sensitivity and selectivity, primarily attributed to their larger active surface area.[39]

**Electrochemical Performance of GDNs**

CV was performed to study the redox and electrochemical characteristics of GDNs. It is well-suited for revealing the electron transfer characteristics, to calculate electrochemical active surface area and showing complete redox activity. CV of the GDNs was executed over a potential range from -0.6 V to 1.0 V, on varying the scan rates from10 $mVs^{-1}$ to 100 $mVs^{-1}$ with 10 mV potential step. The redox activity of GDNs is clearly indicated by the Figure 2a, showing the reduction and oxidation of the $[Fe(CN)_6]^{3-/4-}$ redox system. The ratio of anodic peak current ($I_{pa}$) (249.3 µA) to the cathodic peak current ($I_{pc}$) (-258.4 µA) at scan rate of 50 $mVs^{-1}$ is nearly equals to 1. Similarly, the $I_{pa}/I_{pc}$ is very close to 1 corresponds to a scan rate range of 10 $mVs^{-1}$ to 100 $mVs^{-1}$, indicative of a quasi-reversible profile, and also confirms the electrochemical stability of the fabricated GDNs.[39] These observations suggest that GDNs exhibit remarkable electrocatalytic activity and thereby significantly enhancing the electron transfer rate and electrochemical performance. Figure 2b elucidates that the redox kinetics exhibit a directly proportional relationship with the square root of the scan rate, indicative of Randles–Sevcik behaviour, confirming that the redox reaction is controlled by diffusion process.[40] This Randel-Sevick behaviour is governed by the eq 1:

(1)

where  is the anodic peak current at the given scan rate , ; electroactive surface area, ; electrolyte molar concentration, and ;Diffusion coefficient ($7.6 \times 10^{-6}$ $cm^2s^{-1}$). Moreover, to ensure the high

electroactive surface area of GDNs, it is calculated and compared with unmodified electrodes such as boron doped diamond (BDD) and GCE using eq1, using the peak current values from Figure S2, the electroactive surface area (A) is tabulated in Table S1. on comparison the value of 'A', the active surface area of GDNs is 1.93 times greater than that of BDD and 0.26 times greater than that of GCE.

The shift in redox peak potentials with rise in scan rates is associated with interfacial redox kinetics, which was examined by determining the electron transfer coefficient (α) on applying the Laviron equation, as presented in Figure 2c. Moreover, the linear correlation was established in between log and peak potentials ($E_{pa}$ and $E_{pc}$) as represented by the below mentioned eqs:

$E_{pa} = 0.065 \log + 0.249$ $R^2 = 0.93$ (2)

$E_{pc} = - 0.062 \log + 0.252$ $R^2 = 0.98$ (3)

On comparing the eq. 2 and 3 with the Laviron equations for peak potentials of anodic and cathodic peak [40], we obtain respectively as,

(4)

(5)

Using the eq. 4 and 5, the heterogeneous electron-transfer coefficient (α) was determined to be 0.52, nearly equals to ideal value to 0.5, characteristic of a reversible redox couple exhibiting fast electron transfer kinetics.

In addition, to understand the electronic and ionic contributions at electrode-electrolyte interface, EIS were performed in the frequencies from 0.01 Hz to 100 kHz. Nyquist plot against open circuit potential of redox reaction for GDNs is depicted in Figure 2d. The Nyquist plot was

analysed on the basis of Randles circuit: R(CR)(Q[WR]) as displayed in an inset of Figure 2d. The fitting procedure gives the goodness chi-squared of $6.14 \times 10^{-5}$. The high frequency region consists of ohmic resistance element ($R_s$) that signifies solution resistance equals to 199.9 Ω. The Warburg element, with a value of 504.0 Ω, signifies mass transport impedance, arising from ion diffusion from the bulk to the electrode surface and their migration across the interface. The capacitance (C) corresponds to the electrical double-layer capacitance, which is 20.0 µF for GDNs. The Randles circuit model yields an $R_{ct}$ value of 96.3 Ω, indicating low interfacial resistance and efficient electron transfer, underscoring the GDNs high sensitivity and the significance of its electroactive surface area in governing the kinetics.[41] The observed low charge transfer resistance is primarily because of the high content of $sp^2$-hybridized graphene domains, which provide a higher active surface area and facilitate improved electron transfer kinetics.

**Optimization of Parameters**

To achieve optimal sensitivity and a lower LOD for PQ detection using GDNs, the key parameters need to be optimized include pH, deposition time and deposition potential to maximize DPASV peak current. Among these, electrolyte pH plays a crucial role by affecting the electrode's microstructure and surface chemistry. The DPASV peak current of the GDNs for 10 µM PQ in 0.1M PBS was evaluated in a pH range of 4 to 9. As presented in Figure 3a, the DPASV peak current rose from pH 4 to 6 and then decreased from pH 6 to 8, as illustrated in the inset, indicating that pH influences PQ adsorption on the electrode surface. However, a slight increase in peak current is observed on moving from pH 8 (2.5 µA) to pH 9 (2.8 µA). This might be due to the contribution of $HPO_4^{2-}$ species present in PBS. In phosphate buffers, the dominant species shift with pH. At pH 8-9, the presence of $HPO_4^{2-}$ increases, which can influence the ionic

strength and the double-layer structure at the electrode interface. These changes can affect the mass transport and orientation of paraquat molecules near the electrode surface, potentially enhancing the electrochemical response.[42,43] At low pH, excess $H^+$ ions create a positively charged GDNs surface that repels PQ, limiting its adsorption, while above pH 6.0, the current decreases due to PQ hydrolysis.[44] Therefore, pH 6 was taken as optimal pH to detect PQ on the basis of its large peak current response.

The deposition potential plays a vital role in stripping voltammetry, as shown in Figure 3b, where a distinct PQ peak appears at -0.7 V and increases up to -0.9 V, indicating improved PQ accumulation on GDNs. Beyond -0.9 V, the peak current declines due to excessive $H^+$ generation, which hinders PQ adsorption, making -0.9 V the optimal deposition potential for effective detection.

Optimizing deposition time is essential for maximizing PQ detection sensitivity. As depicted in Figure 3c, the DPASV current response of the GDNs to 10 µM PQ improved with increasing deposition time, peaking at 100 s (as shown in inset), which ensures efficient analyte collection and high sensitivity. Therefore, 100 s was selected as the optimal deposition time for further measurements to balance performance and analysis time.

**DPASV Analysis of PQ**

DPASV was utilized for quantitative analysis due to the necessity of a high current response in such measurements. The PQ detection of was performed using DPASV under optimized conditions in 0.1 M PBS, pH 6, deposition potential of -0.9 V and deposition time of 100 seconds chosen for its highest peak current. Figure 4a shows the DPASV response of 0.1 to 0.8 µM PQ, with rise in current signals appearing around -0.55 V as the PQ concentration increased. Comparable peaks near -0.6 V have been reported in PBS using differential pulse

voltammetry (DPV), confirming the occurrence of redox processes.[45] As the PQ concentration increased, the peak height also rose, indicating enhanced oxidation activity of PQ onto the GDNs surface. Figure 4b demonstrates a linear increase in PQ peak current response in the range of 0.1 to 0.8 µM concentration, following the equation; I (µA) = 0.425 + 3.42C (µM) with a correlation coefficient ($R^2$) of 0.96. The sensitivity of GDNs is determined as 3.42 µA $µM^{-1}$ from the slope of calibration plot, with the detection limit (LOD) values 0.002 µM, based on the 3S/N rule.[40,45,46] Table 1 presents a comparison of the electroanalytical technique, linearity range, and LOD of GDNs compared to those of previously reported electrode materials.

**Selectivity, Repeatability, Stability and Reproducibility Study**

To detect PQ with high specificity, the GDNs should particularly identify PQ amid potential interferents. The selectivity of GDNs was assessed by testing 10 µM PQ in PBS (0.1 M, pH 6) alongside various interfering ions such as magnesium ($Mg^{2+}$), zinc ($Zn^{2+}$), potassium ($K^{+}$), chloride ($Cl^{-}$), acetate, nitrate ($NO^{3-}$), mercuric ($Hg^{2+}$), chromium ($Cr^{3+}$), arsenic ($As^{3+}$), and chemicals for instance, boric acid, ascorbic acid, urea, held at 100 µM, ten times the PQ concentration. The insignificant change in DPASV peak currents response (RSD <5%) is depicted in Figure 4c for in presence of other interferants on GDNs, confirming the high selectivity of GDNs for PQ detection.

The reproducibility of GDNs was determined using 5 different GDNs at 10 µM PQ, resulting in the relative standard deviation (RSD) of 0.9%, as shown in (Figure 4d and S3). Repeatability describes the ability to obtain consistent results across several successive measurements conducted under identical experimental conditions.[47] To assess repeatability, 10 µM PQ was measured using the same GDNs as shown in Figure 4e and Figure S4. Fifty successive measurements produced a low RSD of 1.26%, confirming excellent repeatability.

Notably, there was no requirement to pre-treatment of the electrode surface during the measurements, indicating its strong anti-fouling properties against the PQ redox.[48]

Long-term stability, essential for practical applications, was evaluated by measuring the DPASV peak current at 7-day intervals, showing minimal changes (Figure S5). As shown in Figure 4f, after 49 days of storage in a desiccator at ambient conditions, the GDNs retained 71% of their initial peak current with an RSD of 11.02%, demonstrating high stability.

**DPASV Analysis of Real Sample**

To evaluate the practical feasibility of the proposed GDNs, PQ was detected in the real samples of Amaranthus leaf washed water and seawater. We followed the standard addition method in which PQ was spiked externally, and recovery rates were calculated. Amaranthus leaves were sourced from a local market of Bhubaneswar, Odisha while the seawater sample was collected from Chandrabhaga Beach, Konark, Odisha, India. The results of the PQ analysis in for Amaranthus leaves and seawater sample are displayed in Table S2, indicating satisfying recoveries between 99.7% and 101.5%, with only slight variations from the actual concentration values. The PQ permissible limit sets by United States Environmental Protection Agency for natural water is 0.4 µM.[49] However, the Chinese standard sets the maximum allowable PQ residue in food is 0.78 µM.[49] Figure 5a and Figure 5b illustrate that the GDNs sensor achieves LODs of 0.027 µM, and 0.02 µM for PQ detection in Amaranthus leaves sample and seawater, respectively. The low LODs, well below regulatory limits, confirm the GDN-based sensor's effectiveness for accurate and practical PQ detection in real time environmental monitoring.

To investigate the superiority of the unmodified GDNs sensor over the conventional sensor such as GCE, graphene and BDD electrode, DPASV was performed for 10 µM PQ under optimized

conditions. Figure 6 depicts that the DPASV peak current for GDNs is 37.30 µM, which is about 13 times higher than GCE, 7 times than that of BDD and 3 times greater than graphene. This might be due to the synergy of highly conducting graphene layers and electrochemical stability of diamond. Figure 7 illustrates the possible mechanism of PQ onto GDNs surface. During deposition step of DPASV, $PQ^{2+}$ interacts at the GDNs electrode surface, it gets reduced by the gain of two electrons. These electrons are available as delocalised free electrons in the graphene matrix of GDNs. Furthermore, the polarity of C=O groups present on GDNs (as evidenced by XPS spectrum) might be responsible for the attraction of positively charged $PQ^{2+}$ cation. The reduction primarily takes place because the two quaternary nitrogen atoms in $PQ^{2+}$ are reduced to form $PQ^{0}$. However, the stripping of PQ involves the oxidation of PQ into $PQ^{2+}$by losing electrons. The DPASV peaks in corresponds to $PQ^{2+} + 2e^{-} \rightleftharpoons PQ^{0}$.

The nanoneedles present in GDNs as evidenced by FESEM is responsible for the enhanced aspect ratio. In addition, the nanostructured sharp graphene edges further increase the electroactive sites for the adsorption of analytes. In addition, the STEM, XPS and Raman analyses showed $sp^2$ graphene phases, providing large specific surface area and rapid electron transfer pathway for redox activity at the GDNs-PQ solution interface. Furthermore, the smaller grains of GDNs contribute to enhancing the electrochemical active sited, thereby improving the analyte adsorption. The lower value of $R_{ct}$ for GDNs shows the better electrical conductivity and fast electron transfer of the redox process at GDNs interface. In a nut shell, the hybrid of highly conductive graphene edges with sturdy diamond nanoneedles provides an electrochemical sensor that offers high stability, reliable and reproducible performance for the selective monitoring of toxic PQ for real samples.

## CONCLUSIONS

To summarize, this study finds stable and reliable GDNs for the detection of PQ, which are synthesized using a single-step MPECVD method. The presence of graphene phases encapsulated diamond nanoneedles-like structure enables the enhanced electrochemical performance of GDNs. The diamond-graphene hybrid provides a synergistic role for high electrochemical sensitivity of PQ detection because of the high electrochemical stability with high aspect ratio of diamond nanoneedles and higher conductivity of graphene phases. Under optimized experimental conditions of DPASV, the GDNs showed lower detection limit of 0.002 μM over the linearity from 0.1 to 0.8 μM PQ. Meanwhile, the GDNs exhibited high stability, selectivity, reproducibility and repeatability. In addition, the GDNs showed practical feasibility for PQ detection in real sea water samples and Amaranthus leaves washed water with good recoveries. The contribution of the study suggests that single step MPECVD grown GDNs provides a potential substitute as hybrid electrochemical sensor over the conventional unmodified sensors.

## ASSOCIATED CONTENT

### Supporting Information

The supporting information is available free of charge.

XRD pattern of graphene-encapsulated diamond nanoneedles (GDNs), showing graphene (002) and diamond (111) peaks (Figure S1); cyclic voltammograms of GCE, BDD, and GDNs electrodes in [Fe(CN) ]³ / redox system (Figure S2); reproducibility across 5 electrodes (Figure S3); repeatability across 50 runs (Figure S4); long-term stability over 50 days (Figure S5); electrochemical surface area data and anodic peak currents of GCE, BDD, and GDNs electrodes (Table S1); and recovery results of paraquat in real sample matrices, including sea water and Amaranthus washed water (Table S2).

## AUTHOR INFORMATION


### Corresponding Author

**Kamatchi Jothiramalingam Sankaran**, *Advanced Materials Technology Department, CSIR-Institute of Minerals and Materials Technology, Bhubaneswar-751013, India*
Tel.: +91-6369322495; Email: kjsankaran@immt.res.in

**Ken Haenen**, *Institute for Materials Research (IMO), and IMOMEC, IMEC vzw, Hasselt University, Diepenbeek, 3590, Belgium* Tel.: +3211268875; E-mail: ken.haenen@uhasselt.be

### Authors

**Yogesh Chaudhary-** *CSIR-Institute of Minerals and Materials Technology, Bhubaneswar-751013, India; Academy of Scientific and Innovative Research (AcSIR), Ghaziabad 201002, India.*

**Paulius Pobedinskas-***Institute for Materials Research (IMO), Hasselt University, and IMOMEC, IMEC vzw, 3590 Diepenbeek, Belgium;*

**Rozita Rouzbahani-***Institute for Materials Research (IMO), Hasselt University, and IMOMEC, IMEC vzw, 3590 Diepenbeek, Belgium;*

**Svetlana Korneychuk**-*Electron Microscopy for Materials Science (EMAT), University of Antwerp, 2020 Antwerp, Belgium.*

**Johan Verbeeck**-*Electron Microscopy for Materials Science (EMAT), University of Antwerp, 2020 Antwerp, Belgium.*


### Notes

The authors declare that they have no personal or financial conflicts of interest that could have affected the outcomes or interpretation of the work presented in this manuscript.

**Data availability**

The data supporting the findings of this study will be made available upon reasonable request.

**ACKNOWLEDGEMENTS**

The authors gratefully acknowledge financial support from the Science and Engineering Research Board (SERB), India, and the CSIR-Institute of Minerals and Materials Technology, India, through research projects GAP-336 and OLP-128, as well as the UHasselt-BOF Methusalem NANO project. Yogesh Chaudhary expresses gratitude for the funding received through the CSIR-TWAS Fellowship (Award No. 22/FF/CSIR-TWAS/2022).

**REFERENCES**

(1) Laghrib, F.; Bakasse, M.; Lahrich, S.; El Mhammedi, M. A. Electrochemical Sensors for Improved Detection of Paraquat in Food Samples: A Review. *Mater. Sci. and Eng. C*. Elsevier Ltd, **2020**, *107*, 110349-110358. https://doi.org/10.1016/j.msec.2019.110349.

(2) Jeyapragasam, T.; Raju, R.; Chen, S.-M.; Saraswathi, R.; Hatamleh, A. A.; Chen, T.-W.; Rwei, S.-P. Poly(o-Phenylenediamine)-Multiwalled Carbon Nanotube Nanocomposite Based Electrochemical Sensing Platform for Paraquat Detection. *Int. J. Electrochem. Sci.* **2019**, *14* (8), 8326–8339. https://doi.org/10.20964/2019.08.117.

(3) Chuntib, P.; Themsirimongkon, S.; Saipanya, S.; Jakmunee, J. Sequential Injection Differential Pulse Voltammetric Method Based on Screen Printed Carbon Electrode Modified with Carbon Nanotube/Nafion for Sensitive Determination of Paraquat. *Talanta* **2017**, *170*, 1–8. https://doi.org/10.1016/j.talanta.2017.03.073.

(4) Traiwatcharanon, P.; Siriwatcharapiboon, W.; Jongprateep, O.; Wongchoosuk, C. Electrochemical Paraquat Sensor Based on Lead Oxide Nanoparticles. *RSC Adv.* **2022**, *12* (25), 16079–16092. https://doi.org/10.1039/d2ra02034c.

(5) Rajaram, R.; Neelakantan, L. Recent Advances in Estimation of Paraquat Using Various Analytical Techniques: A Review. *Results Chem.* **2023**, *5,* 100703-100719. https://doi.org/10.1016/j.rechem.2022.100703.

(6) Chen, L.; Na, R.; Boldt, E.; Ran, Q. NLRP3 Inflammasome Activation by Mitochondrial Reactive Oxygen Species Plays a Key Role in Long-Term Cognitive Impairment Induced by Paraquat Exposure. *Neurobiol. Aging* **2015**, *36* (9), 2533–2543. https://doi.org/10.1016/j.neurobiolaging.2015.05.018.

(7) Narasimhan, M.; Riar, A. K.; Rathinam, M. L.; Vedpathak, D.; Henderson, G.; Mahimainathan, L. Hydrogen Peroxide Responsive MiR153 Targets Nrf2/ARE Cytoprotection in Paraquat Induced Dopaminergic Neurotoxicity. *Toxicol. Lett.* 2014, *228* (3), 179–191. https://doi.org/10.1016/j.toxlet.2014.05.020.

(8) Baltazar, M. T.; Dinis-Oliveira, R. J.; de Lourdes Bastos, M.; Tsatsakis, A. M.; Duarte, J. A.; Carvalho, F. Pesticides Exposure as Etiological Factors of Parkinson's Disease and Other Neurodegenerative Diseases-A Mechanistic Approach. *Toxicol. Lett.* **2014**, *230* (2), 85–103. https://doi.org/10.1016/j.toxlet.2014.01.039.

(9) Sun, J.; Guo, F.; Shi, Q.; Wu, H.; Sun, Y.; Chen, M.; Diao, G. Electrochemical Detection of Paraquat Based on Silver Nanoparticles/Water-Soluble Pillar[5]Arene Functionalized Graphene Oxide Modified Glassy Carbon Electrode. *J. of Electroanal. Chem.* **2019**, *847*, 113221113229. https://doi.org/10.1016/j.jelechem.2019.113221.

(10) Zhang, Y.; Huang, Y.; Fu, L.; Qiu, J.; Wang, Z.; Wu, A. Colorimetric Detection of Paraquat in Aqueous and Fruit Juice Samples Based on Functionalized Gold Nanoparticles. *J. of Food Compos. and Anal.* **2020**, *92*, 103574-103596. https://doi.org/10.1016/j.jfca.2020.103574.

(11) Zhao, Z.; Zhang, F.; Zhang, Z. A Facile Fluorescent "Turn-off" Method for Sensing Paraquat Based on Pyranine-Paraquat Interaction. *Spectrochim. Acta A Mol Biomol. Spectrosc.* **2018**, *199*, 96–101. https://doi.org/10.1016/j.saa.2018.03.042.

(12) Luo, H.; Wang, X.; Huang, Y.; Lai, K.; Rasco, B. A.; Fan, Y. Rapid and Sensitive Surface-Enhanced Raman Spectroscopy (SERS) Method Combined with Gold Nanoparticles for Determination of Paraquat in Apple Juice. *J. Sci. Food Agric.* **2018**, *98* (10), 3892–3898. https://doi.org/10.1002/jsfa.8906.

(13) Lamei, N.; Ezoddin, M.; Kakavandi, N. R.; Abdi, K.; Ghazi-khansari, M. Ultrasound-Assisted Switchable Solvent in Determination of Quaternary Ammonium Herbicide Paraquat in Biological, Environmental Water, and Apple Juice Samples Using Chemical Reduction Process Coupled to GC–MS Detection. *Chromatographia* **2018**, *81* (6), 923–930. https://doi.org/10.1007/s10337-018-3500-x.

(14) Rashidipour, M.; Heydari, R.; Maleki, A.; Mohammadi, E.; Davari, B. Salt-Assisted Liquid–Liquid Extraction Coupled with Reversed-Phase Dispersive Liquid–Liquid Microextraction for Sensitive HPLC Determination of Paraquat in Environmental and Food Samples. *J. of Food Meas. and Character.* **2019**, *13* (1), 269–276. https://doi.org/10.1007/s11694-018-9941-y.

(15) Hassan, M. H.; Khan, R.; Andreescu, S. Advances in Electrochemical Detection Methods for Measuring Contaminants of Emerging Concerns. *Electrochem. Sci. Adv.* John Wiley and Sons Inc., **2022,** *2*, 1-27 https://doi.org/10.1002/elsa.202100184.

(16) Kumunda, C.; Adekunle, A. S.; Mamba, B. B.; Hlongwa, N. W.; Nkambule, T. T. I. Electrochemical Detection of Environmental Pollutants Based on Graphene Derivatives: A Review. *Front. in Mater.* Frontiers Media S.A. **2021,** *7,* 616787-616817. https://doi.org/10.3389/fmats.2020.616787.

(17) Potes-Lesoinne, H. A.; Ramirez-Alvarez, F.; Perez-Gonzalez, V. H.; Martinez-Chapa, S. O.; Gallo-Villanueva, R. C. Nanomaterials for Electrochemical Detection of Pollutants in Water: A Review. *Electrophor.*. John Wiley and Sons Inc, **2022**, *43*, 249–262. https://doi.org/10.1002/elps.202100204.

(18) Barbosa, P. F. P.; Vieira, E. G.; Cumba, L. R.; Paim, L. L.; Nakamura, A. P. R.; Andrade, R. D. A.; do Carmo, D. R. Voltammetric Techniques for Pesticides and Herbicides Detection- an Overview. *Int. J. Electrochem. Sci.* **2019**, *14* (4), 3418–3433. https://doi.org/10.20964/2019.04.60.

(19) Kadu, R. D.; Keri, R. S.; Nagaraju, D. H.; Budagumpi, S. State-of-the-Art Electrochemical Sensors for Quantitative Detection of Pesticides. *App. Organometal. Chem*. John Wiley and Sons Ltd **2023**, *37*, 7097-7177. https://doi.org/10.1002/aoc.7097.

(20) Song, D.; Wang, Y.; Lu, X.; Gao, Y.; Li, Y.; Gao, F. Ag Nanoparticles-Decorated Nitrogen-Fluorine Co-Doped Monolayer MoS2 Nanosheet for Highly Sensitive

Electrochemical Sensing of Organophosphorus Pesticides. *Sens. Actuators B Chem.* **2018**, *267*, 5–13. https://doi.org/10.1016/j.snb.2018.04.016.

(21) Xie, Y.; Gao, F.; Tu, X.; Ma, X.; Xu, Q.; Dai, R.; Huang, X.; Yu, Y.; Lu, L. Facile Synthesis of MXene/Electrochemically Reduced Graphene Oxide Composites and Their Application for Electrochemical Sensing of Carbendazim. *J. Electrochem. Soc.* **2019**, *166* (16), B1673–B1680. https://doi.org/10.1149/2.0091916jes.

(22) Mariyappan, V.; Keerthi, M.; Chen, S. M. Highly Selective Electrochemical Sensor Based on Gadolinium Sulfide Rod-Embedded RGO for the Sensing of Carbofuran. *J. Agric. Food Chem.* **2021**, *69* (9), 2679–2688. https://doi.org/10.1021/acs.jafc.0c07522.

(23) Xiao, F.; Li, H.; Yan, X.; Yan, L.; Zhang, X.; Wang, M.; Qian, C.; Wang, Y. Graphitic Carbon Nitride/Graphene Oxide(g-C3N4/GO) Nanocomposites Covalently Linked with Ferrocene Containing Dendrimer for Ultrasensitive Detection of Pesticide. *Anal. Chim. Acta* **2020**, *1103*, 84–96. https://doi.org/10.1016/j.aca.2019.12.066.

(24) Wang, Q.; Zhangsun, H.; Zhao, Y.; Zhuang, Y.; Xu, Z.; Bu, T.; Li, R.; Wang, L. Macro-Meso-Microporous Carbon Composite Derived from Hydrophilic Metal-Organic Framework as High-Performance Electrochemical Sensor for Neonicotinoid Determination. *J. Hazard. Mater.* **2021**, *411,* 125122-125134. https://doi.org/10.1016/j.jhazmat.2021.125122.

(25) Tan, X.; Zhang, Z.; Cao, T.; Zeng, W.; Huang, T.; Zhao, G. Control Assembly of Pillar[6]Arene-Modified Ag Nanoparticles on Covalent Organic Framework Surface for Enhanced Sensing Performance toward Paraquat. *ACS Sustain. Chem. Eng.* **2019**, *7* (24), 20051–20059. https://doi.org/10.1021/acssuschemeng.9b05804.

(26) Tcheumi, H. L.; Tassontio, V. N.; Tonle, I. K.; Ngameni, E. Surface Functionalization of Smectite-Type Clay by Facile Polymerization of β-Cyclodextrin Using Citric Acid Cross Linker: Application as Sensing Material for the Electrochemical Determination of Paraquat. *Appl Clay Sci.* **2019**, *173*, 97–106. https://doi.org/10.1016/j.clay.2019.03.013.

(27) Einaga, Y. Diamond Electrodes for Electrochemical Analysis. *J. Appl. Electrochem.* **2010**, *40* (10), 1807–1816. https://doi.org/10.1007/s10800-010-0112-z.

(28) Banerjee, D.; Sankaran, K. J.; Deshmukh, S.; Ficek, M.; Yeh, C. J.; Ryl, J.; Lin, I. N.; Bogdanowicz, R.; Kanjilal, A.; Haenen, K.; Sinha Roy, S. Single-Step Grown Boron Doped Nanocrystalline Diamond-Carbon Nanograss Hybrid as an Efficient Supercapacitor Electrode. *Nanoscale* **2020**, *12* (18), 10117–10126. https://doi.org/10.1039/d0nr00230e.

(29) Baig, N.; Waheed, A.; Sajid, M.; Khan, I.; Kawde, A. N.; Sohail, M. Porous Graphene-Based Electrodes: Advances in Electrochemical Sensing of Environmental Contaminants. *Trends in Environ. Analyt. Chem*. Elsevier B.V., **2021,** *30*, 120-134. https://doi.org/10.1016/j.teac.2021.e00120.

(30) Chaudhary, Y.; Suman, S.; Sankaran, K. J. Superior Electrochemical Performance of Doped Porous Graphene Electrode for Supercapacitor and Paraquat Detection. *Microchemical Journal* **2025**, *213*, 113780. https://doi.org/10.1016/j.microc.2025.113780.

(31) Catania, F.; Marras, E.; Giorcelli, M.; Jagdale, P.; Lavagna, L.; Tagliaferro, A.; Bartoli, M. A Review on Recent Advancements of Graphene and Graphene-Related Materials in Biological Applications. *App. Sci. (Switzerland)*. *MDPI AG,* **2021**, *11*, 614–634. https://doi.org/10.3390/app11020614.

(32) Williams, O. A.; Douhéret, O.; Daenen, M.; Haenen, K.; Osawa, E.; Takahashi, M. Enhanced Diamond Nucleation on Monodispersed Nanocrystalline Diamond. *Chem. Phys. Lett.* **2007**, *445* (4–6), 255–258. https://doi.org/10.1016/j.cplett.2007.07.091.

(33) Sankaran, K. J.; Ficek, M.; Kunuku, S.; Panda, K.; Yeh, C. J.; Park, J. Y.; Sawczak, M.; Michałowski, P. P.; Leou, K. C.; Bogdanowicz, R.; Lin, I. N.; Haenen, K. Self-Organized Multi-Layered Graphene-Boron-Doped Diamond Hybrid Nanowalls for High-Performance Electron Emission Devices. *Nanoscale* **2018**, *10* (3), 1345–1355. https://doi.org/10.1039/c7nr06774g.

(34) Banerjee, D.; Sankaran, K. J.; Deshmukh, S.; Yeh, C. J.; Gupta, M.; Lin, I. N.; Haenen, K.; Kanjilal, A.; Sinha Roy, S. Single-Step Synthesis of Core-Shell Diamond-Graphite Hybrid Nano-Needles as Efficient Supercapacitor Electrode. *Electrochim. Acta* **2021**, *397*, 139267-139275. https://doi.org/10.1016/j.electacta.2021.139267.

(35) Yu, S.; Sankaran, K. J.; Korneychuk, S.; Verbeeck, J.; Haenen, K.; Jiang, X.; Yang, N. High-Performance Supercabatteries Using Graphite@diamond Nano-Needle

Capacitor Electrodes and Redox Electrolytes. *Nanoscale* **2019**, *11* (38), 17939–17946. https://doi.org/10.1039/c9nr07037k.

(36) Sankaran, K. J.; Yeh, C. J.; Hsieh, P. Y.; Pobedinskas, P.; Kunuku, S.; Leou, K. C.; Tai, N. H.; Lin, I. N.; Haenen, K. Origin of Conductive Nanocrystalline Diamond Nanoneedles for Optoelectronic Applications. *ACS Appl. Mater. Interfaces* **2019**, *11* (28), 25388–25398. https://doi.org/10.1021/acsami.9b05469.

(37) Tulić, S.; Waitz, T.; Čaplovičová, M.; Habler, G.; Varga, M.; Kotlár, M.; Vretenár, V.; Romanyuk, O.; Kromka, A.; Rezek, B.; Skákalová, V. Covalent Diamond-Graphite Bonding: Mechanism of Catalytic Transformation. *ACS Nano* **2019**, *13* (4), 4621–4630. https://doi.org/10.1021/acsnano.9b00692.

(38) Carvalho, A. F.; Holz, T.; Santos, N. F.; Ferro, M. C.; Martins, M. A.; Fernandes, A. J. S.; Silva, R. F.; Costa, F. M. Simultaneous CVD Synthesis of Graphene-Diamond Hybrid Films. *Carbon N Y* **2016**, *98*, 99–105. https://doi.org/10.1016/j.carbon.2015.10.095.

(39) Guo, Y.; Huang, N.; Yang, B.; Wang, C.; Zhuang, H.; Tian, Q.; Zhai, Z.; Liu, L.; Jiang, X. Hybrid Diamond/Graphite Films as Electrodes for Anodic Stripping Voltammetry of Trace $Ag^{+}$ and $Cu^{2+}$ *Sens. Actuators B Chem.* **2016**, *231*, 194–202. https://doi.org/10.1016/j.snb.2016.02.098.

(40) Sain, S.; Roy, S.; Mathur, A.; Rajesh, V. M.; Banerjee, D.; Sarkar, B.; Roy, S. S. Electrochemical Sensors Based on Flexible Laser-Induced Graphene for the Detection of Paraquat in Water. *ACS Appl Nano Mater.* **2022**, *5* (12), 17516–17525. https://doi.org/10.1021/acsanm.2c02948.

(41) Siuzdak, K.; Ficek, M.; Sobaszek, M.; Ryl, J.; Gnyba, M.; Niedziałkowski, P.; Malinowska, N.; Karczewski, J.; Bogdanowicz, R. Boron-Enhanced Growth of Micron-Scale Carbon-Based Nanowalls: A Route toward High Rates of Electrochemical Biosensing. *ACS Appl. Mater. Interfaces* **2017**, *9* (15), 12982–12992. https://doi.org/10.1021/acsami.6b16860.

(42) Liu, T.; Xue, Q.; Jia, J.; Liu, F.; Zou, S.; Tang, R.; Chen, T.; Li, J.; Qian, Y. New Insights into the Effect of PH on the Mechanism of Ofloxacin Electrochemical Detection in Aqueous Solution. *Phy. Chem. Chemical Physics* **2019**, *21* (29), 16282–16287. https://doi.org/10.1039/c9cp03486b.

(43) Zhang, J.; Lin, Z.; Qin, Y.; Li, Y.; Liu, X.; Li, Q.; Huang, H. Fabricated Electrochemical Sensory Platform Based on the Boron Nitride Ternary Nanocomposite Film Electrode for Paraquat Detection. *ACS Omega* **2019**, *4* (19), 18398–18404. https://doi.org/10.1021/acsomega.9b02658.

(44) Saidin, M. I.; Isa, I. M.; Rosmi, M. S.; Hashim, N.; Ahmad, M. S.; Mohd Yazid, S. N. A.; Kuppan, S.; Yii, M. W.; Bahari, A. A. Revolutionising Pesticide Detection: A High-Sensitivity Electrochemical Sensor with CdS/g-$C_3N_4$/MWCNTs for Paraquat Monitoring. *Int. J. Environ. Anal. Chem.* **2024,** *1*, 1–15. https://doi.org/10.1080/03067319.2024.2356032.

(45) Zhang, H.; Huang, K. T.; Ding, L.; Yang, J.; Yang, Y. W.; Liang, F. Electrochemical Determination of Paraquat Using a Glassy Carbon Electrode Decorated with Pillararene-Coated Nitrogen-Doped Carbon Dots. *Chinese Chem. Letters* **2022**, *33* (3), 1537–1540. https://doi.org/10.1016/j.cclet.2021.09.002.

(46) Hou, E.; Kong, Z.; Wu, J.; Wang, H.; Nie, P.; Lu, M.; Chang, L. Preparation of Ag–$TiO_2$/MXene Composite Material for Electrochemical Detection of Paraquat. *J. of Mater. Sci.: Mater. in Electron.* **2023**, *34* (14), 1177-1189. https://doi.org/10.1007/s10854-023-10603-7.

(47) Zhou, M.; Tang, T.; Qin, D.; Cheng, H.; Wang, X.; Chen, J.; Wågberg, T.; Hu, G. Hematite Nanoparticle Decorated MIL-100 for the Highly Selective and Sensitive Electrochemical Detection of Trace-Level Paraquat in Milk and Honey. *Sens. Actuators B Chem.* **2023**, *376,* 132931-132642. https://doi.org/10.1016/j.snb.2022.132931.

(48) Pop, A.; Lung, S.; Orha, C.; Manea, F. Silver/Graphene-Modified Boron Doped Diamond Electrode for Selective Detection of Carbaryl and Paraquat from Water. *Int. J. Electrochem Sci.* **2018**, *13* (3), 2651–2660. https://doi.org/10.20964/2018.03.02.

(49) Wiwasuku, T.; Chuaephon, A.; Habarakada, U.; Boonmak, J.; Puangmali, T.; Kielar, F.; Harding, D. J.; Youngme, S. A Water-Stable Lanthanide-Based MOF as a Highly Sensitive Sensor for the Selective Detection of Paraquat in Agricultural Products. *ACS Sustain. Chem. Eng.* **2022**, *10* (8), 2761–2771. https://doi.org/10.1021/acssuschemeng.1c07966.

(50) Sain, S.; Ficek, M.; Olejnik, A.; Sawczak, M.; Bogdanowicz, R.; Roy, S. S. Direct Determination of Paraquat Herbicide by Square-Wave Voltammetry by Two-Step

Transfer Mechanism at Heterogeneous Boron-Doped Carbon Nanowall Electrodes. *Diam. Relat. Mater.* **2023**, *140,* 110504-110515. https://doi.org/10.1016/j.diamond.2023.110504.

(51) Ribeiro, J. A.; Carreira, C. A.; Lee, H. J.; Silva, F.; Martins, A.; Pereira, C. M. Voltammetric Determination of Paraquat at DNA-Gold Nanoparticle Composite Electrodes. In *Electrochim. Acta*; **2010**, *55*, 7892–7896. https://doi.org/10.1016/j.electacta.2010.03.058.

(52) Pop, A.; Lung, S.; Orha, C.; Manea, F. Silver/Graphene-Modified Boron Doped Diamond Electrode for Selective Detection of Carbaryl and Paraquat from Water. *Int. J. Electrochem. Sci.* **2018**, *13* (3), 2651–2660. https://doi.org/10.20964/2018.03.02.

(53) Pop, A.; Manea, F.; Flueras, A.; Schoonman, J. Simultaneous Voltammetric Detection of Carbaryl and Paraquat Pesticides on Graphene-Modified Boron-Doped Diamond Electrode. *Sensors (Switzerland)* **2017**, *17* (9) 2033-2043. https://doi.org/10.3390/s17092033.

(54) Zhou, H.; Wang, Y.; Xu, L.; Zhou, Y.; Hong, Y.; Hou, D.; Liao, X. Facile Preparation of Ultra Stable Polymer-Based Sensor for Highly Sensitive and Selective Detection of Paraquat in Agricultural Products. *Microchemical Journal,* **2024**, *199* 110097-110107. https://doi.org/10.1016/j.microc.2024.110097.

(55) Li, J.; Lei, W.; Xu, Y.; Zhang, Y.; Xia, M.; Wang, F. Fabrication of Polypyrrole-Grafted Nitrogen-Doped Graphene and Its Application for Electrochemical Detection of Paraquat. *Electrochim. Acta* **2015**, *174*, 464–471. https://doi.org/10.1016/j.electacta.2015.06.028.

**Table 1. Comparative PQ Detection of the GDNs Electrode with Previously Fabricated Electrodes**

| Electrode materials | Electroanalytical techniques | Linear range (µM) | LOD (µM) | Ref. |
|---|---|---|---|---|
| [a]t-LIG | SWV | 0.5–35 | 0.54 | 40 |
| [b]CdS/g-$C_3N_4$/MWCNTs PE | SWV | 1.0–100 | 0.14 | 44 |
| [c]CCDs/GCE | DPV | 0.1–10 | 0.064 | 45 |

| | | | | |
|---|---|---|---|---|
| [d]B: CNW | SWV | 0.1–1, 2–12 | 0.47 | [50] |
| [e]Au NPs/DNA/GE | DPV | 5−1000 | 1.3 | [51] |
| [f]BDDGRAg | DPV | 0.2–1.2 | 0.0011 | [52] |
| [g]BDDGR | DPV | 0.2–1.2 | 0.04 | [53] |
| [h]Nf-Gr-MWCNTs-COOH | SWV | 0.01–15 | 0.005 | [54] |
| [i]PPY-NGE/GCE | DPV | 0.05–2 0 | 0.041 | [55] |
| GDNs | DPASV | 0.1–0.8 | 0.002 | This work |

[a]treated LIG; [b]multiwalled carbon nanotubes and cadmium sulphide on graphitic carbon nitride; [c]modified glassy carbon electrode with nitrogen-doped carbon dots; [d]Boron-doped carbon nanowalls; [e]Au NPs−DNA-modified gold electrode; [f]Silver/graphene-modified; [g]graphene-modified boron-doped diamond electrode; [h]Nafion modified with graphene; [i]Polypyrrole-grafted nitrogen-doped graphene GCE

## Figure captions

**Figure 1.** (a) FESEM micrograph of GDNs which shows cross-sectional FESEM micrograph as an inset (I), (b) The Raman spectrum of GDNs in which the inset shows the C1s XPS spectrum of GDNs, (c) Cross-sectional bright-field STEM micrograph of GDNs on a Si substrate and (d) and the inset of (d) the typical HAADF-STEM images of GDNs.

**Figure 2.** Electrochemical characterizations of GDNs (a) CVs of GDNs in 5 mM $[Fe(CN)_6]^{3-/4-}$ solution and 0.1M KCl at varying scan rates from 10 $mVs^{-1}$ to 100 $mVs^{-1}$, (b) Calibration curve of

Peak currents of CVs verses square root of scan rates, (c) Laviron plot and (d) Nyquist Plot in which the Randles circuit is shown as an inset.

**Figure 3.** Optimization of DPASV parameters for 10 μM of PQ (a) pH of 0.1M PBS solution as supporting electrolyte, which shows the calibration plot of peak current at different pH as an inset, (b) deposition potential at pH=6 and the inset representing the peak current against the varying deposition potential, (c) deposition time at pH=6 and deposition potential= -0.9 V where the inset shows the enlarged view of peak current and the calibration plot of peak current with varying deposition time.

**Figure 4.** (a) DPASV curves of PQ in 0.1M PBS at pH=6; deposition potential=-0.9 V and deposition time = 150 s, (b) calibration curve of peak current verses PQ concentration, (c) Peak current responses of GDNs in presence of interfering agents, (d) Peak current responses of 5 GDNs for 10 μM of PQ, (e) Peak current response of 50 successive DPASV measurements for 10 μM of PQ, (f) current responses of GDNs for 50 days with an interval of 7 days for 10 μM of PQ.

**Figure 5.** (a) DPASV for different concentration of PQ in sea water whereas the inset shows the linear fit of peak current on varying concentration, (b) DPASV for different concentration of PQ in Amaranthus leaves washed water whereas the inset shows the linear fit of peak current on varying concentration.

**Figure 6.** DPASV comparison of different electrodes for 10 μM PQ under optimized conditions.

**Figure 7.** Schematic showing paraquat redox mechanism at GDNs.

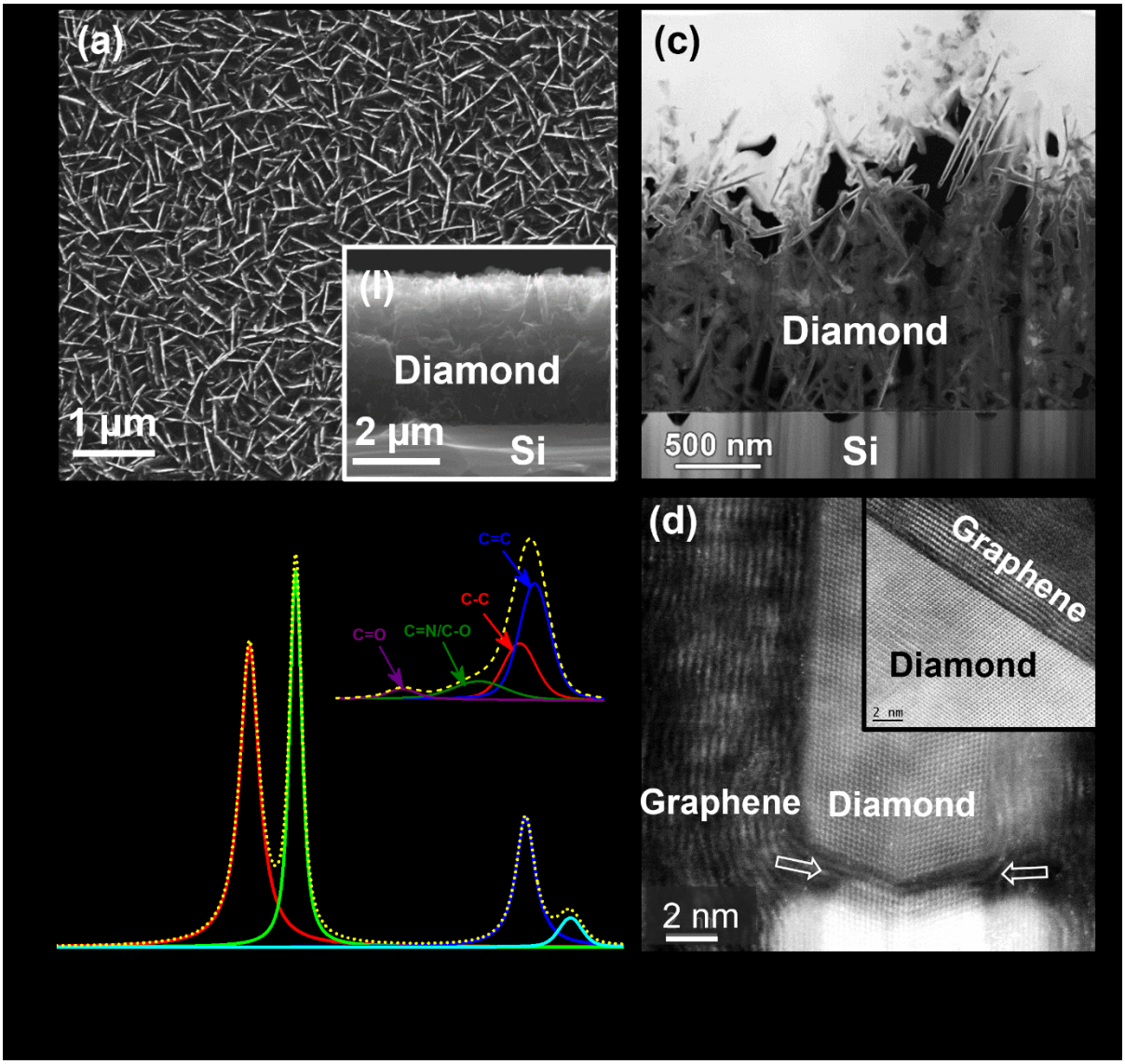
(a)
1 μm
(I)
Diamond
2 μm
Si
(c)
Diamond
500 nm
Si
C=C
C-C
C=O
C=N/C-O
(d)
Graphene
Diamond
2 nm
Graphene
Diamond
2 nm

**Figure 1.**

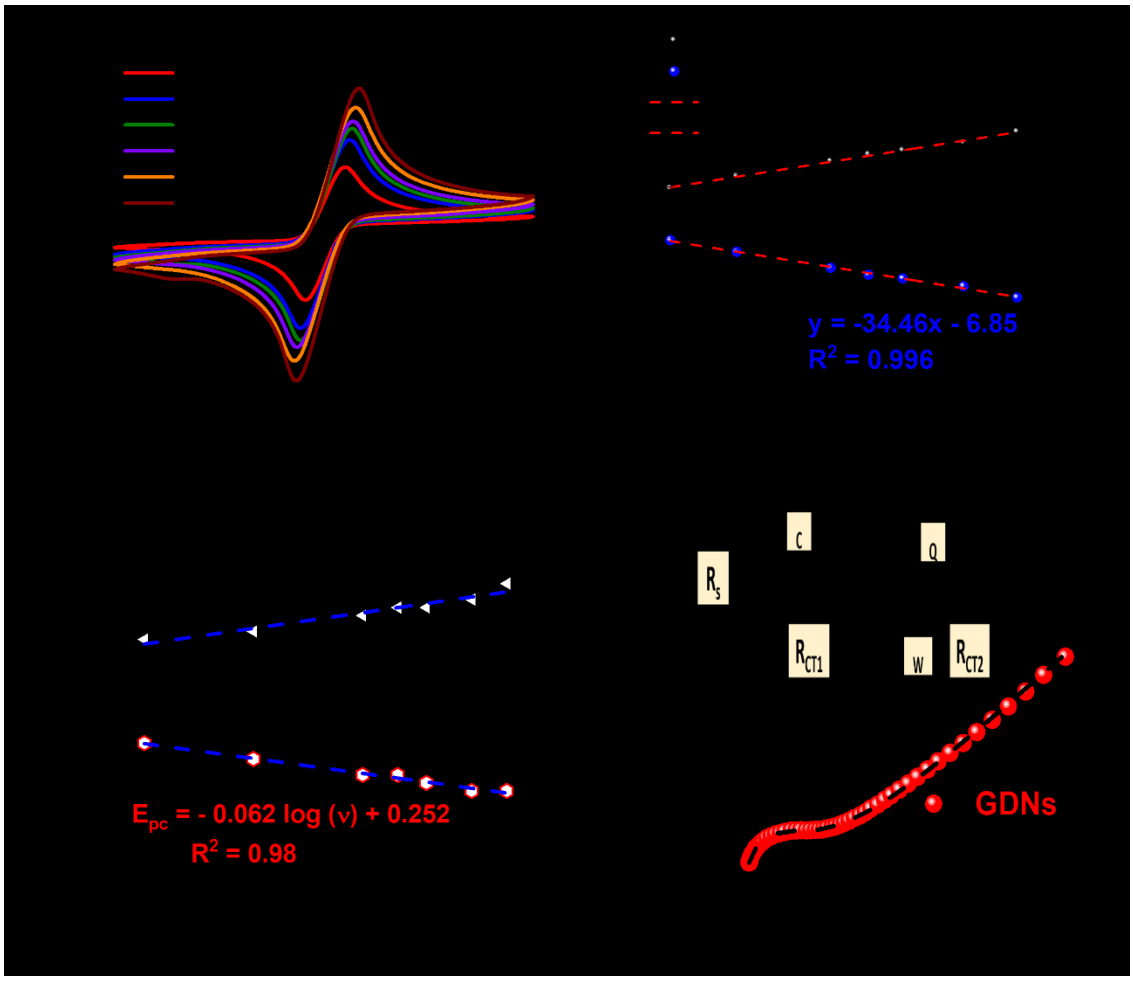
y = -34.46x - 6.85
R2 = 0.996
C
Q
Rs
RCT1
W
RCT2
GDNs
Epc = - 0.062 log (ν) + 0.252
R2 = 0.98

**Figure 2.**

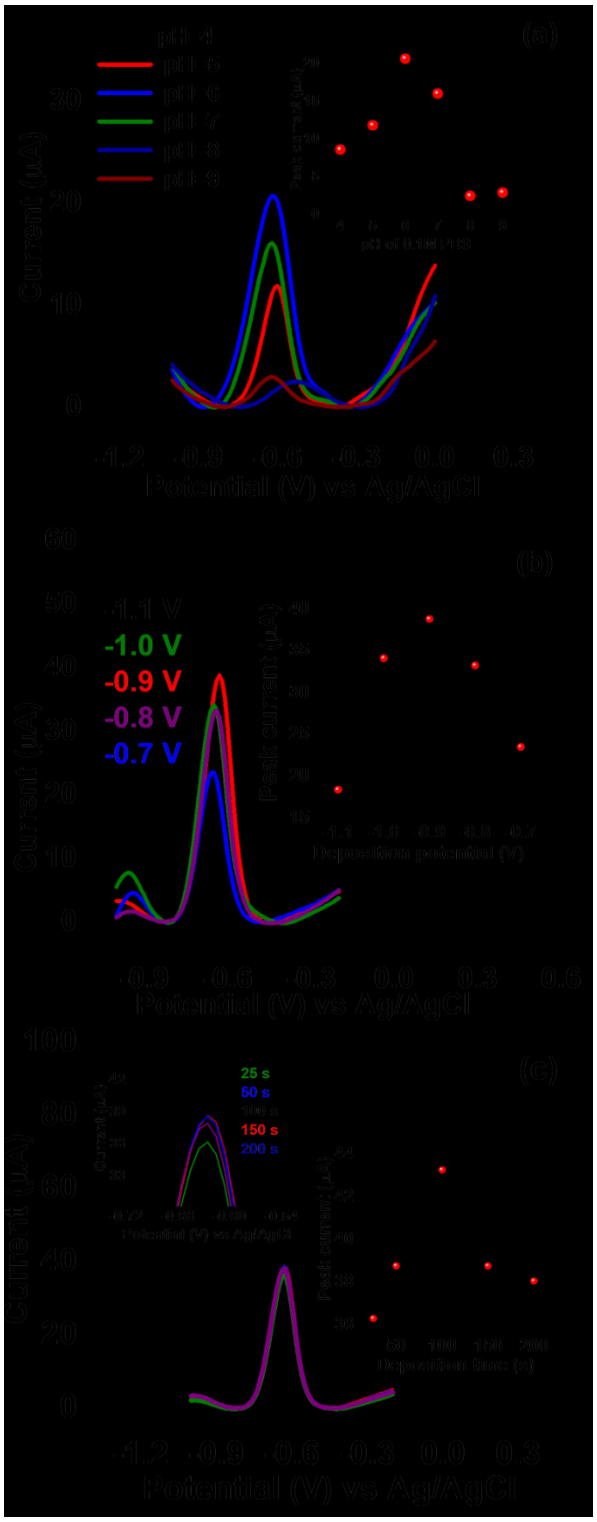
(a)
pH 4
pH 5
pH 6
pH 7
pH 8
pH 9
Current (μA)
Potential (V) vs Ag/AgCl
(b)
-1.1 V
-1.0 V
-0.9 V
-0.8 V
-0.7 V
Peak current (μA)
Deposition potential (V)
Current (μA)
Potential (V) vs Ag/AgCl
(c)
25 s
50 s
100 s
150 s
200 s
Peak current (μA)
Deposition time (s)
Current (μA)
Potential (V) vs Ag/AgCl

**Figure 3.**

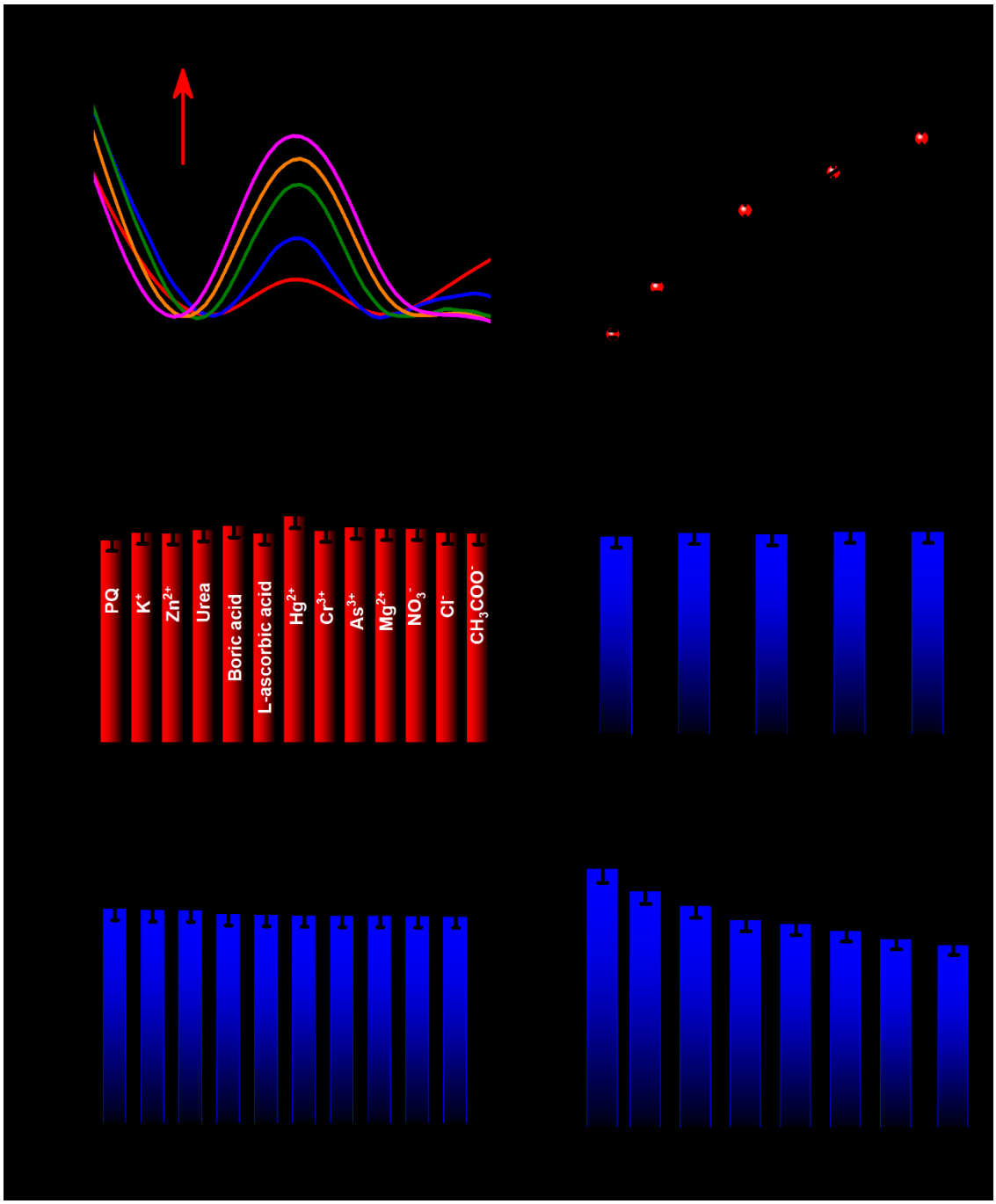
PQ
K+
Zn2+
Urea
Boric acid
L-ascorbic acid
Hg2+
Cr3+
As3+
Mg2+
NO3-
Cl-
CH3COO-

**Figure 4.**

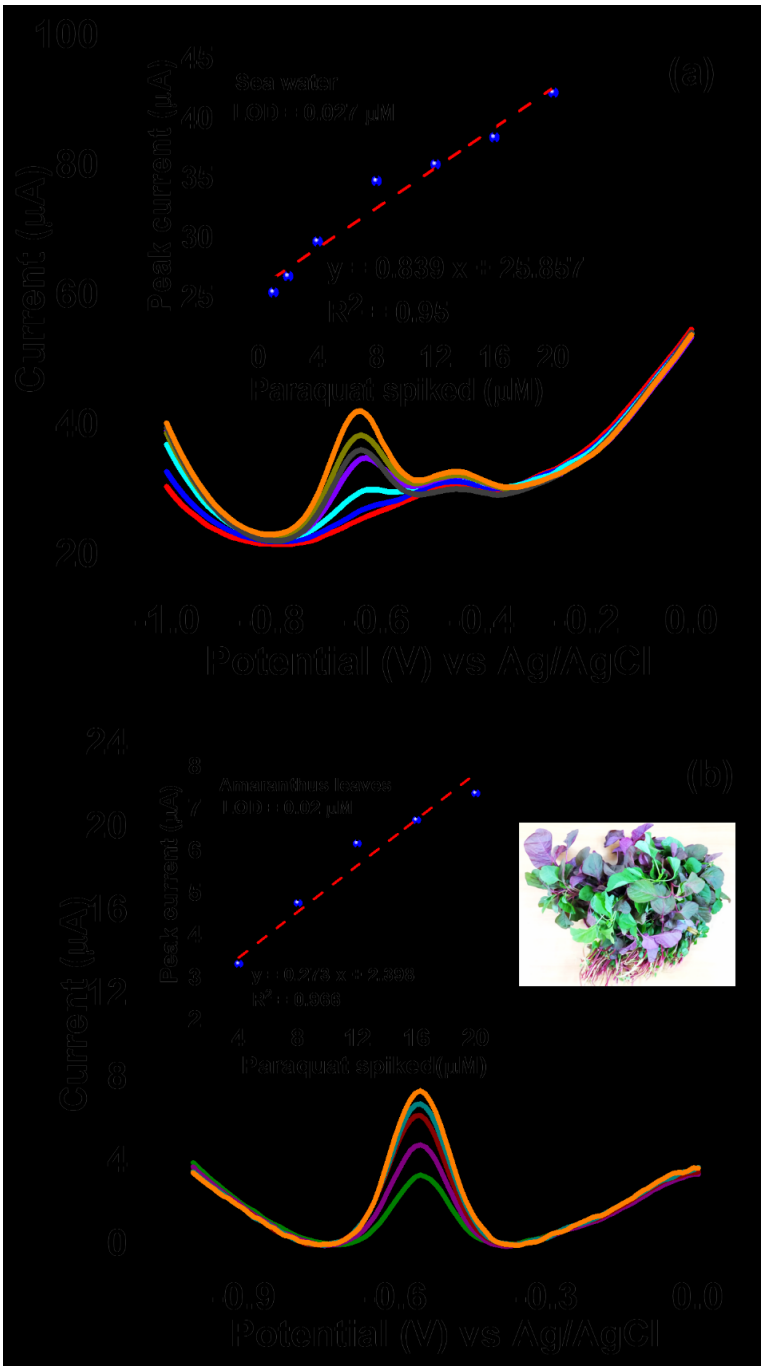
(a)
Sea water
LOD : 0.027 µM
y : 0.839 x + 25.857
R² : 0.95
Peak current (µA)
Paraquat spiked (µM)
Current (µA)
Potential (V) vs Ag/AgCl
(b)
Amaranthus leaves
LOD : 0.02 µM
y : 0.273 x + 2.393
R² : 0.966
Peak current (µA)
Paraquat spiked(µM)
Current (µA)
Potential (V) vs Ag/AgCl

**Figure 5.**

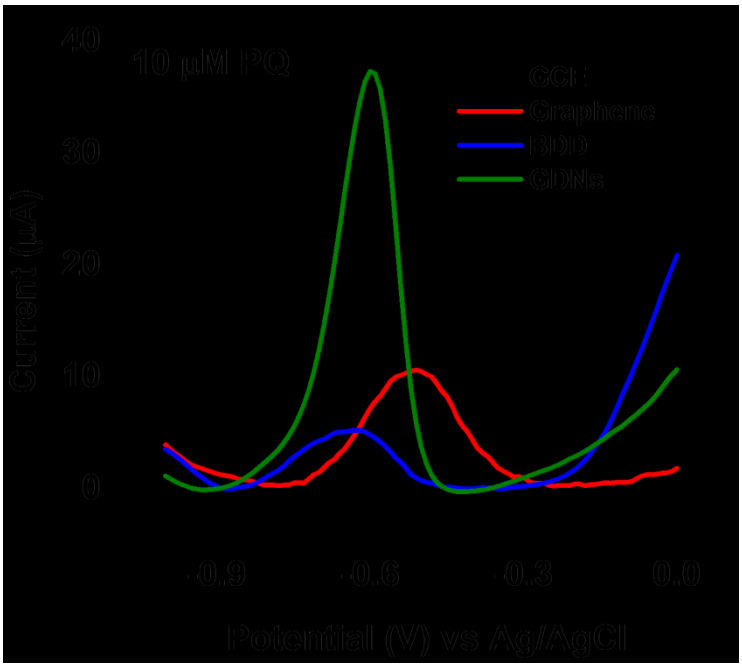


**Figure 6.**

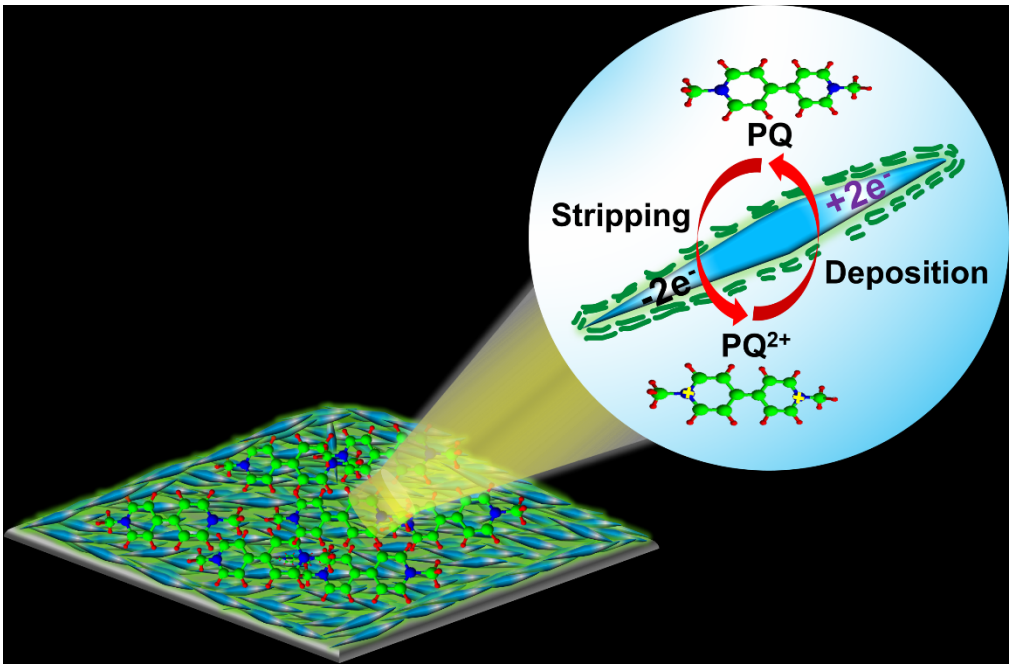


**Figure 7.**